Viscoelastic flows of a lid-driven cavity using spectral element methods

D. Fenton [a,*], P.J. Bowen [a], E. De Angelis [b,*]

[a] *Cardiff University, School of Engineering, The Parade, Cardiff, CF24 3AA, United Kingdom*
[b] *Università di Bologna, Dipartimento di Ingegneria Industriale, Forlì, 47121, Italy*

ARTICLE INFO

ABSTRACT

The performance of a spectral element method in the DEVSS-G formulation for the solution of non-Newtonian flows is assessed by means of a systematic analysis of the benchmark lid-driven cavity problem. It is first validated by comparison with the creeping Newtonian and Oldroyd-B flows, where in the latter case a lid velocity regularisation scheme must be employed to remove the singularity at the lid-wall interfaces. In both instances, excellent agreement is found with the literature for stable, time-independent flows, and in fact it is shown that higher Weissenberg numbers can be obtained using the present methodology for these types of flow. Some physical aspects of the solutions are also presented and discussed, however at increasing Weissenberg numbers, the methodology breaks down due to a lack of convergence in the BDF/FPI time advancement scheme. By systematically assessing the effects of the levels of hp-refinement and temporal refinement on the flow fields, as well as the introduction of the extension-limiting Giesekus mobility parameter in the constitutive equations, it is demonstrated that in each instance the inability to accurately resolve the stress gradients leads to a compounding of errors in the BDF/FPI regime, ultimately causing it to diverge.

1. Introduction

The computational study of viscoelastic flows presents difficulties predominantly on two fronts; the rheological model used to relate the elastic stress to the deformation, and the numerical method used to approximate the solution. The practice of using benchmark problems to validate the accuracy of numerical methods owes itself to the fact that there are very few analytical solutions available for viscoelastic flows. Being of simple geometry, the lid-driven cavity is one such numerical benchmark that has been extensively studied, however more so in the Newtonian regime. In two dimensions, the geometry of the problem is that of a closed rectangle of height H and length L, with one wall moving parallel to itself whilst keeping the domain in tact as shown schematically in Fig. 1. The fluid within forms the closed system to be studied. The flow is characterised by the Reynolds number, $\mathrm{Re} = \rho U H / \eta$, with density ρ, dynamic viscosity η and characteristic velocity and length scales U and H; all of these are kept constant here. Beginning with the work of Kawaguti in 1961 [1], the Newtonian problem has been used not only as a numerical benchmark for many decades [2,3], but as insight into the plethora of fundamental fluid mechanical phenomena which arise due to its discontinuous velocity boundary conditions where the lid and two of the stationary walls meet, as observed experimentally [4].

The predominant feature of the flow is the primary recirculation region. Under creeping flow conditions $\mathrm{Re} \rightarrow 0$, due to the linearity

of the Stokes flow equations this region is fore-aft symmetric about the line $x/L = 0.5$. Further to the main circulation, there exists a mathematically infinite geometric sequence of increasingly smaller Moffat eddies [5] in both of the lower corners C and D in Fig. 1; the debate as to whether this sequence is indeed physically infinite is not the subject of this study. Increasing the Reynolds number breaks the fore-aft symmetry by moving the primary vortex centre towards corner B, until a critical Reynolds number at which experimentally the flow becomes three-dimensional and then time-dependent [6].

The literature for the study of viscoelastic fluids is more sparse than that of the Newtonian problem. Viscoelasticity introduces two further flow parameters which define the flow, namely the Deborah number $\mathrm{De} = \lambda U / L$ and the Weissenberg number $\mathrm{We} = \lambda U / H$, where λ is the relaxation time of the fluid. In the case of the square cavity $L = H$, these two definitions are identical. The effect of viscoelasticity on the system has also been shown experimentally to break the fore-aft symmetry by increasing the wall velocity (thus increasing De and We), however moving the primary vortex centre towards corner A rather than B as in the increased Re case, and will eventually lead to a purely elastic flow instability which causes the stable flow to break down [7].

While there exist several numerical studies concerned with the lid-driven cavity flow of viscoelastic fluids with constant viscosity, they overwhelmingly use finite difference (FD) [8,9], finite element

---

* Corresponding authors.
E-mail addresses: fentond@cardiff.ac.uk (D. Fenton), e.deangelis@unibo.it (E. De Angelis).
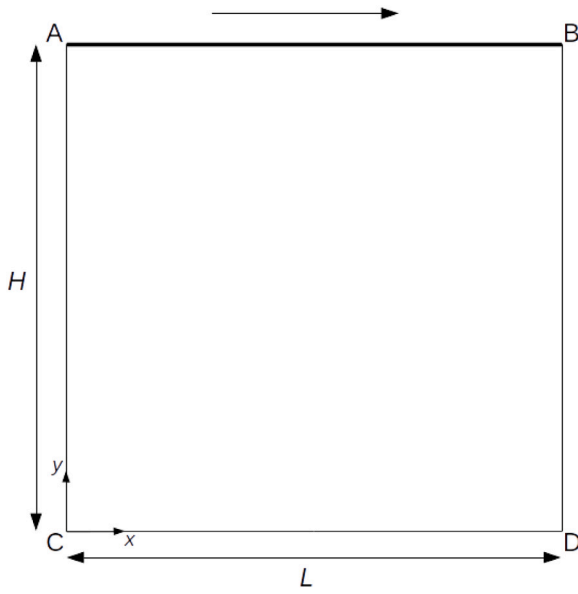
Fig. 1. Schematic of the lid-driven cavity with length L and height H.

(FE) [10,11] or finite volume (FV) [12,13] methods, which rely on incredibly fine meshes in order to obtain convergence. In this study, a high-order spectral elements method (SEM) will be employed. While there have been SEM Newtonian studies utilising the lid-driven cavity, for example the adaptive mesh refinement validation of Henderson [14], literature on such a SEM viscoelastic study could not be found at the time of writing. Techniques for improving stabilisation in the referenced FD, FE and FV studies include log-conformation, kernel-conformation and the first-order upwind approximation; the approach of the present work, however, was to utilise a variation of the DEVSS-G formulation of the constitutive equations and employ the discontinuous Galerkin method on the discretised elastic stress. The code used is adapted from that of Kynch [15], the original version of which is available at: https://github.com/rosskynch/DG_DEVSSG_SEM_Axi.

2. Governing equations

2.1. Navier–Stokes and rheology

An incompressible, isothermal, viscoelastic flow is considered in the present study. The conservation of momentum in dimensionless form with no external forces acting is given by

$$\text{Re}\frac{D\mathbf{u}}{Dt} = -\nabla p + \beta\nabla^2\mathbf{u} + \nabla \cdot \boldsymbol{\tau}, \tag{1}$$

where the fields are velocity $\mathbf{u}$, pressure p and elastic stress $\boldsymbol{\tau}$. The dimensionless quantity β is the ratio of solvent to total solvent-plus-polymer viscosity. The statement of incompressibility can be formulated as per Gwynllyw and Phillips [16] by consideration of the pressure average on the domain Ω, and is given by

$$-\nabla \cdot \mathbf{u} = \mu \int_\Omega p\,\mathrm{d}\Omega, \tag{2}$$

where $\mu > 0$ is a constant. This is shown to be equivalent to the typical statement of incompressibility, $\nabla \cdot \mathbf{u} = 0$, by integrating both sides of Eq. (2) over Ω and implementing Green's theorem on the right hand side. This formulation is used in order to remove the indeterminacy in the pressure, and so that the pressure decomposition is consistent with the solution space upon discretisation.

In order to close the system, a constitutive equation is required relating the elastic stress to the rate of deformation, $\mathbf{d} = \frac{1}{2}((\nabla\mathbf{u})+(\nabla\mathbf{u})^T)$.

The rheology used for the present study is the Oldroyd-B model [17] for a viscoelastic fluid,

$$\boldsymbol{\tau} + \text{We}\,\overset{\triangledown}{\boldsymbol{\tau}} = 2(1-\beta)\mathbf{d} \tag{3}$$

where $\overset{\triangledown}{\boldsymbol{\tau}}$ is the upper-convected derivative of the elastic stress tensor, given by

$$\overset{\triangledown}{\boldsymbol{\tau}} = \frac{\partial\boldsymbol{\tau}}{\partial t} + \mathbf{u} \cdot \nabla\boldsymbol{\tau} - \boldsymbol{\tau} \cdot (\nabla\mathbf{u}) - (\nabla\mathbf{u})^T \cdot \boldsymbol{\tau}. \tag{4}$$

It is worth noting that the Oldroyd-B model exhibits an infinite extensional viscosity $\eta_{ext} = N_1/4\dot{\varepsilon}$ at a finite extensional strain rate $\dot{\varepsilon}$, where $N_1 = \tau_{xx} - \tau_{yy}$ is the first normal stress difference, occurring at $\dot{\varepsilon} = 1/2\text{We}$. This implies an infinite first normal stress difference, which is clearly unphysical, and an undesirable property of the model particularly when dealing with highly extensional flows such as the lid-driven cavity. For this reason, the Giesekus model is also briefly considered [18], as it does not suffer this issue. The constitutive equation is given by

$$\boldsymbol{\tau} + \text{We}\left(\overset{\triangledown}{\boldsymbol{\tau}} + \frac{\alpha}{1-\beta}\boldsymbol{\tau}^2\right) = 2(1-\beta)\mathbf{d}, \tag{5}$$

where $\alpha > 0$ is the mobility parameter, and the Oldroyd-B model is recovered by setting it equal to zero.

2.2. DEVSS-G formulation

In order to improve the stability of the discretised system, the governing equations are written in a modified form. The velocity gradient tensor, here denoted $\nabla\mathbf{u} = \mathbf{G}$, is introduced as a variable in the momentum Eq. (1) as per a variation of the DEVSS-G [19] method, proposed by Bogaerds et al. [20], leaving the constitutive equation to be solved directly. This improves the ellipticity of the system, thus improving stability. The momentum Eq. (1) under this formulation becomes

$$\text{Re}\frac{D\mathbf{u}}{Dt} = -\nabla p + \nabla \cdot \boldsymbol{\tau} + (\beta + \theta)\nabla^2\mathbf{u} - \theta\nabla \cdot \mathbf{G}, \tag{6}$$

where θ is chosen to be equal to $(1-\beta)$ in order to make the coefficient of $\nabla^2\mathbf{u}$ unity; since $\nabla \cdot \mathbf{G} = \nabla^2\mathbf{u}$, it is straightforward to see that Eqs. (1) and (6) are identical. This is different to the original DEVSS-G formulation in that the stabilising term is the velocity gradient as opposed to the rate of strain tensor $\mathbf{d}$. This choice appears more natural than the original formulation for this problem, since the enforcement of incompressibility ensures that $\nabla \cdot (\nabla\mathbf{u})^T = 0$ in the momentum Eq. (1); otherwise, the Laplacian in the momentum Eq. (1) would contain the rate of strain tensor $\nabla \cdot (\nabla\mathbf{u} + (\nabla\mathbf{u})^T)$ instead. Thus, the enforcement of incompressibility encourages the use of this alternative DEVSS-G formulation.

3. Geometry and problem formulation

The geometry of the present work is that of the two-dimensional lid-driven cavity on the domain $0 \le x \le L$, $0 \le y \le \Lambda L$. For the present work, the aspect ratio Λ is equal to one; it is worth noting that in this case and only this case, the Weissenberg number and Deborah number are equivalent, since $\text{De} = \Lambda\text{We}$. The boundary Γ is decomposed into two distinct regions,

$$\Gamma = \Gamma^W \cup \Gamma^L, \tag{7}$$

where Γ^W and Γ^L are the stationary wall and moving lid boundaries respectively. In the case of the single-lid cavity, the boundary Γ^W lies on $x = 0$, $x = L$ and $y = 0$, and the boundary Γ^L on $y = L$.

No-slip velocity conditions are prescribed on the entire boundary Γ such that

$$\mathbf{u} = \mathbf{0} \text{ on } \Gamma^W, \tag{8}$$

and

$$\mathbf{u} = \mathbf{u}_L(\mathbf{x}) \text{ on } \Gamma^L, \tag{9}$$

where $\mathbf{u}_L(\mathbf{x})$ is the velocity of the lid. The classic lid-driven cavity problem consists of a lid of constant non-zero velocity in the x-direction only, however the singularities that arise on the interface between Γ^W and Γ^L with the boundary conditions given by (8) and (9) if $\mathbf{u}_L$ is constant and non-zero would cause exceedingly strong numerical instabilities due to the infinite acceleration at these points. Theoretically, this leads to an infinite extensional rate du/dx locally, and even though the numerical approximation introduces a degree of local smoothing dependent on the mesh resolution (as the velocity increases from $\mathbf{0}$ to $\mathbf{u}_L$ over a finite distance δx), for the viscoelastic models considered here previous studies have been unable to deal with the resulting stress peaks in these localised regions, and fail to converge for all but essentially-Newtonian fluids of near-zero Weissenberg number [12]. For this reason, the lid velocity is regularised such that the velocity vanishes on the interface between Γ^W and Γ^L. A generalisation of the common quartic regularisation is as follows:

$$u_L(x) = \begin{cases} [U/\delta^2(1-\delta)^2](x/L)^2(1-x/L)^2 & \text{for } 0 \le x/L \le \delta \\ U & \text{for } \delta < x/L < 1-\delta \\ [U/\delta^2(1-\delta)^2](x/L)^2(1-x/L)^2 & \text{for } 1-\delta \le x/L \le 1, \end{cases} \tag{10}$$

where $u_L(x)$ is the x-component of the lid velocity $\mathbf{u}_L = u_L(x)\hat{\mathbf{x}}$ and U is the peak lid velocity. The dimensionless quantity δ is the fraction of L over which each quartic velocity region occurs, with $\delta = 0$ corresponding to the unregularised problem and $\delta = 0.5$ to a smooth quartic lid velocity profile. It is the peak velocity U that is used to characterise flow quantities such as the Weissenberg number. For completeness, the y-component of the lid velocity v_L is zero in all cases. As $\delta \to 0$ one would anticipate a stronger similarity with the idealised problem and a reduction in the maximum attainable Weissenberg number. In the regularised instances, the velocity and velocity gradient vanish at the walls and the velocity profiles are continuous, however the velocity gradient of any regularisation except for $\delta = 0.5$ is not continuous at the points where the quartic sections of the velocity profile transition to a constant — that is to say, the boundary conditions exhibit a $C1$ discontinuity at $x/L = \delta$. This is significant when choosing the discretisation scheme in a spectral elements study, since $C1$ continuity is naturally not enforced across elemental boundaries anyway, as discussed in Section 4.2.

4. Numerical discretisation

The following description of the temporal and spatial discretisation schemes used follows those presented by Kynch and Phillips [15].

4.1. Temporal discretisation

The system is discretised uniformly in time by considering a time step Δt such that the nth time step is $t^n = n\Delta t$. The evaluation of a function $\mathbf{f}(\mathbf{x}, t)$ at the nth time step is denoted $\mathbf{f}^n = \mathbf{f}(\mathbf{x}, t^n)$. The velocity–pressure equations are decoupled from the constitutive equation by evaluating $\nabla \cdot \boldsymbol{\tau}$ in the momentum equation explicitly. The DEVSS-G term in (6) is further decoupled from the velocity–pressure equations and also treated explicitly. These explicit terms are extrapolated using a second-order method (EX2) such that an arbitrary function $\mathbf{F}(\mathbf{x}, t)$ at time t^{n+1} is approximated by

$$\mathbf{F}^{n+1} \approx \sum_{q=0}^{1} \beta_q \mathbf{F}^{n-q}, \tag{11}$$

where $\beta_0 = 2$, $\beta_1 = -1$ are the second order extrapolation coefficients.

The material derivative present in the DEVSS-G momentum equation is approximated by a second-order Operator-Integration-Factor

Splitting scheme (OIFS2), which reduces multiple operator problems to an associated set of initial value subproblems [21], given by

$$\frac{D\mathbf{u}}{Dt} \approx \frac{1}{\Delta t}\left(\gamma_0 \mathbf{u}^{n+1} - \sum_{q=0}^{1} \alpha_q \tilde{\mathbf{u}}_q^{n+1}\right), \tag{12}$$

where $\gamma_0 = 3/2$, $\alpha_0 = 2$ and $\alpha_1 = 1/2$ are the OIFS2 coefficients. The terms $\tilde{\mathbf{u}}_q^{n+1}$ are solutions to the pure-advection initial value problems associated with the OIFS scheme, and their solutions are obtained using an RK4 scheme. In effectively decoupling the convection and Stokes operators in this OIFS scheme, a larger CFL number is allowed than more traditional semi-implicit schemes such as BDF while maintaining stability [22], improving computational time-to-solution by allowing larger time step sizes. Furthermore, this characteristic-based formulation is well suited for convection-dominated problems, which occur in the instance of high Reynolds and Weissenberg numbers, the latter of which is of interest for this study [21].

The resulting hybrid OIFS2/EX2 temporally-discretised velocity–pressure equations are thus given by

$$\frac{\mathrm{Re}\gamma_0}{\Delta t}\mathbf{u}^{n+1} - (\beta+\theta)\nabla^2\mathbf{u}^{n+1} + \nabla p^{n+1} =$$
$$\sum_{q=0}^{1}\left(\frac{\mathrm{Re}}{\Delta t}\alpha_q\tilde{\mathbf{u}}_q^{n+1} + \beta_q(\nabla\cdot\boldsymbol{\tau}^{n-q} - \theta\nabla\cdot\mathbf{G}^{n-q})\right), \tag{13}$$

$$\nabla \cdot \mathbf{u}^{n+1} + \mu \int_\Omega p^{n+1} d\Omega = 0. \tag{14}$$

A similar methodology can be used to derive the temporally-discretised constitutive equation from (3), utilising a second-order backward difference formula (BDF2) in place of OIFS2. The resulting second-order BDF/EX scheme leads to the semi-discrete constitutive equation given by

$$\left(1 + \mathrm{We}\frac{\gamma_0}{\Delta t}\right)\boldsymbol{\tau}^{n+1} - \mathrm{We}\left(\boldsymbol{\tau}^{n+1}\cdot\nabla\mathbf{u}^{n+1} + (\nabla\mathbf{u}^{n+1})^T\cdot\boldsymbol{\tau}^{n+1}\right)$$
$$= 2(1-\beta)\mathbf{d}^{n+1} + \mathrm{We}\sum_{q=0}^{1}\left(\frac{\alpha_q}{\Delta t}\boldsymbol{\tau}^{n-q} - \beta_q\mathbf{u}^{n+1}\cdot\nabla\boldsymbol{\tau}^{n-q}\right)$$
$$- \mathrm{We}\frac{\alpha}{1-\beta}\sum_{q=0}^{1}\beta_q(\boldsymbol{\tau}^{n-q})^2. \tag{15}$$

An additional stability improvement is implemented via a fixed-point iteration (FPI) *within* each time step, which increases the maximum attainable Weissenberg number while making only a minor addition to the computational resources required compared to the more straightforward BDF/EX methodology [15]. One defines $\tilde{\boldsymbol{\tau}}^0 = \boldsymbol{\tau}^n$, and iteratively solves the BDF2/FPI system

$$\left(1 + \mathrm{We}\frac{\gamma_0}{\Delta t}\right)\tilde{\boldsymbol{\tau}}^{i+1} - \mathrm{We}\left(\tilde{\boldsymbol{\tau}}^{i+1}\cdot\nabla\mathbf{u}^{n+1} + (\nabla\mathbf{u}^{n+1})^T\cdot\tilde{\boldsymbol{\tau}}^{i+1}\right)$$
$$= 2(1-\beta)\mathbf{d}^{n+1} + \mathrm{We}\left(\sum_{q=0}^{1}\left(\frac{\alpha_q}{\Delta t}\boldsymbol{\tau}^{n-q}\right) - \mathbf{u}^{n+1}\cdot\nabla\tilde{\boldsymbol{\tau}}^i\right) \quad (16)$$
$$- \mathrm{We}\frac{\alpha}{1-\beta}(\tilde{\boldsymbol{\tau}}^i)^2,$$

until $|\tilde{\boldsymbol{\tau}}^{i+1} - \tilde{\boldsymbol{\tau}}^i| < \phi$, where ϕ is some threshold value. Once this has been reached, $\boldsymbol{\tau}^{n+1}$ is set equal to $\tilde{\boldsymbol{\tau}}^{i+1}$. The time-marching algorithm is terminated when $S^n < \epsilon$, where S^n is a convergence parameter given by

$$S^n = \frac{1}{\Delta t}\sqrt{\frac{\|p^n - p^{n-1}\|^2 + \|\mathbf{u}^n - \mathbf{u}^{n-1}\|^2 + \|\boldsymbol{\tau}^n - \boldsymbol{\tau}^{n-1}\|^2}{\|p^n\|^2 + \|\mathbf{u}^n\|^2 + \|\boldsymbol{\tau}^n\|^2}} \tag{17}$$

and ϵ is a threshold value used to determine when a steady-state solution has been reached.

4.2. Spatial discretisation

4.2.1. Momentum equation

The spatial discretisation is obtained by implementing the spectral element method (SEM). The global physical domain Ω is discretised into K non-overlapping elements, such that $\Omega = \cup_{k=1}^{K} \Omega_k$, allowing any integral across the global domain to be decomposed into contributions over each local element. Each contribution is then transformed to a reference element, D, via the Jacobian J^k [23,24]. The field variables are then decomposed within the reference element into a spectrum of basis functions interpolated with respect to the Gauss–Lobatto-Legendre points for improved stability with respect to a uniform spacing, such that

$$u_a^k(\xi, \eta) = \sum_{i=0}^{N} \sum_{j=0}^{N} \left(u_{ij}^k\right)_a h_i(\xi) h_j(\eta), \tag{18}$$

$$p^k(\xi, \eta) = \sum_{i=1}^{N-1} \sum_{j=1}^{N-1} p_{ij}^k \tilde{h}_i(\xi) \tilde{h}_j(\eta), \tag{19}$$

where u_a^k represents the a-component of the vector field within an element k. $h_i(\xi)$ and $\tilde{h}_i(\xi)$ are respectively the velocity and pressure basis functions, defined in terms of the Legendre polynomial of degree N, $L_N(x)$, by

$$h_i(\xi) = -\frac{(1 - \xi^2)L_n'(\xi)}{N(N+1)L_N(\xi_i)(\xi - \xi_i)} \qquad 0 \le i \le N, \tag{20}$$

and

$$\tilde{h}_i(\xi) = -\frac{(1 - \xi_i^2)L_n'(\xi)}{N(N+1)L_N(\xi_i)(\xi - \xi_i)} \qquad 1 \le i \le N - 1, \tag{21}$$

where ξ_q is the qth GLL point in one direction.

The spectral decomposition within each element of the velocity gradient $\mathbf{G}$ is obtained by consideration of the internal GLL nodes only, $1 \le q \le N-1$, in the same manner as the pressure, such that the spectral representation of the ab component of $\mathbf{G}$ within a local element is given by

$$\mathbf{G}_{ab}^k(\xi, \eta) = \sum_{i=1}^{N-1} \sum_{j=1}^{N-1} (G_{ij}^k)_{ab} \tilde{h}_i(\xi) \tilde{h}_j(\eta). \tag{22}$$

This means that $\mathbf{G}$ itself can be calculated within each element independently of adjacent elements, improving computational efficiency and stability [25]. Multiplying the definition $\mathbf{G} = \nabla \mathbf{u}$ by a test function ϕ, integrating over the global domain and decomposing into contributions over each local element, one obtains for the ab component

$$\left(\sum_{k=1}^{K} \int_{\Omega_k} \mathbf{G} : \phi d\Omega \right)_{ab} = \left(\sum_{k=1}^{K} \int_{\Omega_k} (\nabla \mathbf{u}) : \phi d\Omega \right)_{ab}. \tag{23}$$

By use of the GLL quadrature rules, which accurately approximate the definite integral of a function as a weighted sum of function values at the GLL points, the spectral representation of $\mathbf{G}$ can be written locally as a linear system for each component ab as

$$\tilde{M}^k \mathbf{G}_{ab}^k = \hat{\mathbf{d}}_{ab}^k, \tag{24}$$

where $\tilde{M}^k$ is the local mass matrix and the vector $\hat{\mathbf{d}}_{ab}^k$ contains the contributions of the ab velocity gradient component at each GLL point. The solution to the local $\mathbf{G}$ is then fed back into the velocity–pressure system.

4.2.2. Constitutive equation

The constitutive equation is solved spatially at each GLL point separately within each local element, with the values of the velocity gradient and the previous time step elastic stress determining the constituent parameters of the rheological system. The spectral decomposition of the elastic stress can therefore be represented as

$$\tau_{ab}^k(\xi, \eta) = \sum_{i=0}^{N} \sum_{j=0}^{N} \left(\tau_{ab}^k\right)_{ij} h_i(\xi) h_j(\eta). \tag{25}$$

This leaves the convective term $\mathbf{u} \cdot \nabla \tau$, which by construction of the velocity decomposition possesses a coupling between the elements. This is treated by utilising the Discontinuous Galerkin (DG) method [26,27], in particular the streamline upwind method, which allows the stress to be discontinuous across the elements. Thus, the only interaction of stress between elements is that which occurs on the elemental boundary. Multiplying the convective term by a test function $\mathbf{S}$, integrating over Ω and applying the decomposition principle, the convective derivative can be written

$$\int_{\Omega} (\mathbf{u} \cdot \nabla \tau) : \mathbf{S} d\Omega = \sum_{k=1}^{K} \int_{\Omega_k} (\mathbf{u} \cdot \nabla \tau) : \mathbf{S} d\Omega_k. \tag{26}$$

By application of the divergence theorem to the right hand side, one obtains

$$\sum_{k=1}^{K} \int_{\Omega_k} (\mathbf{u} \cdot \nabla \tau) : \mathbf{S} d\Omega_k = \sum_{k=1}^{K} \int_{\Gamma_k} (\mathbf{n} \cdot \mathbf{u}) \tau : \mathbf{S} d\Gamma_k - \sum_{k=1}^{K} \int_{\Omega_k} (\mathbf{u} \cdot \nabla \mathbf{S}) : \tau d\Omega_k. \tag{27}$$

Since the stress is allowed to be discontinuous across an element boundary, the value of the stress on a particular boundary point is not necessarily the same when evaluated using the approximations in either adjoining element. Denoting the value of the stress on the boundary as evaluated in one element by τ^e (external stress) and the value as evaluated on the same point in the adjacent element by τ^i (internal stress), one can define the boundary stress as

$$\tau = \begin{cases} \alpha_{DG} \tau^e + (1 - \alpha_{DG}) \tau^i & \text{on } \Gamma_k^- \\ \alpha_{DG} \tau^i + (1 - \alpha_{DG}) \tau^e & \text{on } \Gamma_k^+ \end{cases} \tag{28}$$

for DG upwinding parameter $0 \le \alpha_{DG} \le 1$, where $\alpha_{DG} = 1$ corresponds to the fully upwinded case. Substituting this into (27), applying integration by parts and the divergence theorem again yields

$$\sum_{k=1}^{K} \int_{\Omega_k} (\mathbf{u} \cdot \nabla \tau) : \mathbf{S} d\Omega_k = \sum_{k=1}^{K} \int_{\Omega_k} (\mathbf{u} \cdot \nabla \tau) : \mathbf{S} d\Omega_k$$
$$+ \alpha_{DG} \sum_{k=1}^{K} \int_{\Gamma_k^-} (\mathbf{n} \cdot \mathbf{u})[\tau] : d\Gamma_k$$
$$+ (1 - \alpha_{DG}) \sum_{k=1}^{K} \int_{\Gamma_k^+} (\mathbf{n} \cdot \mathbf{u})[\tau] : d\Gamma_k, \tag{29}$$

where $[\tau] = \tau^e - \tau^i$ is the difference in stress between elements.

Introducing the intermediate variable $\hat{\tau} = \mathbf{u} \cdot \nabla \tau$, discretisation of the DG convective term leads to the linear system

$$M^k \hat{\tau}_{ab}^k = \hat{E}^k \tau_{ab}^k + (B_{DG}^k)_{ab}, \tag{30}$$

where

$$M^k \hat{\tau}_{ab}^k \approx \left(\int_D \hat{\tau}^k(\xi, \eta) : \mathbf{S} \det \mathbf{J}^k d\xi d\eta \right)_{ab}, \tag{31}$$

$$\hat{E}^k \tau_{ab}^k \approx \left(\int_D (\mathbf{u}^k \cdot \nabla \tau^k) : \mathbf{S} \det \mathbf{J}^k d\xi d\eta \right)_{ab}, \tag{32}$$

and

$$(B_{DG}^k)_{ab} \approx \left(\sum_{m=1}^{4} \int_{D_m^-} (\mathbf{n}^{k_m} \cdot \mathbf{u}^k)[\tau^k] : \mathbf{S} \det \mathbf{J}^{k_m} d\xi \right)_{ab}. \tag{33}$$

Here, the sum over m is over the four edges of the parent element and the Jacobian $\mathbf{J}^{k_m}$ is that of the mapping of edge m of the physical element edge to the parent element, since $(B_{DG}^k)_{ab}$ contains the term over the boundary integral. For a detailed treatise and full derivation of the above, see the description of Owens and Phillips [28]. The matrix M^k is diagonal, thus making the system trivial to solve. The global matrix for the velocity–pressure system is then assembled by summing contributions over each element, accounting for the shared boundaries, and inserting the known boundary conditions where necessary.
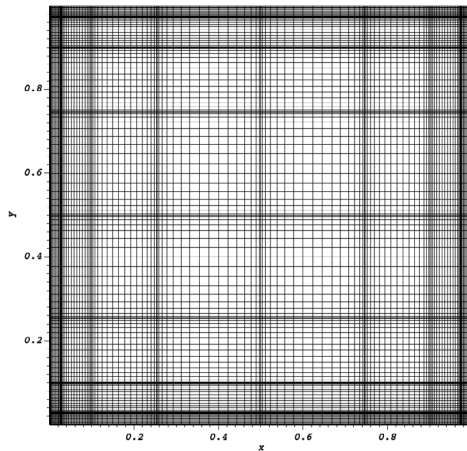
(a) $m = 8$, $N = 16$.
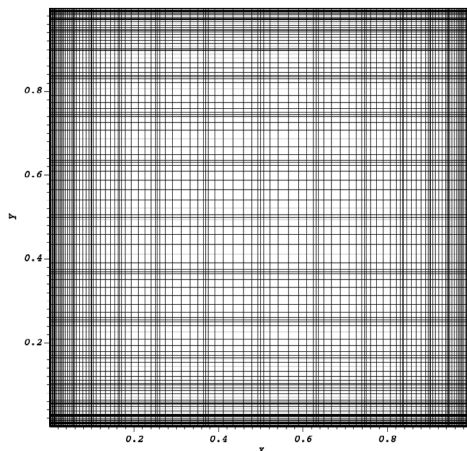
(b) $m = 16$, $N = 8$.

Fig. 2. Representative GLL meshes.

5. Results

5.1. Mesh and parameterisation

In order to capture the effects at the walls and lid more accurately, the elemental mesh is refined at these surfaces. For a mesh of $K = m \times m$ elements, a mapping from a uniform set of elemental gridpoints $a_i = i/(m+1)$ to a graded set q_i, both on the interval $[0, 1]$, is used to achieve this in both the x and y directions, where i are the integers running from 0 to $m + 1$. In the present study, the symmetrical refinement mapping is given by

$$q_i = \frac{1}{2} \left(1 + \frac{\tanh\left(\beta_a(2a_i - 1)\right)}{\tanh \beta_a} \right), \tag{34}$$

where β_a is a constant stretching parameter. The choice of β_a is made such that for a given number of elements the $C1$ discontinuities in the velocity profile at $x/L = \delta$ and $1 - \delta$ falls upon an elemental boundary. The number of elements in each direction m is also kept even to ensure that an elemental boundary falls on the centrelines.

Three meshes are used in the present study, with $m = 8, 16$ and 20, each with β_a chosen to place the $i = 2, 4$ and 6 elemental gridpoints

Table 1

Comparison of the literature with the current study for a creeping Newtonian flow with the unregularised lid $\delta = 0$. Minimum values of u are computed along $x/L = 0.5$, and maximum values of v are computed along $y/L = 0.5$. The centre of the primary vortex for each study is also compared.

Reference	u_{min}/U	v_{max}/U	x_c/L	y_c/L
Sahin, Owens [13]	−0.207754	0.186273	0.5000	0.7626
Yapici et al. [8]	−0.207738	0.184427	0.5000	0.7651
Sousa et al. [12]	−0.207762	0.184449	0.5000	0.7647
Current study	−0.207639	0.182273	0.5000	0.7628

Table 2

Effect of regularisation on u_{min}/U along $x/L = 0.5$ and v_{max}/U along $y/L = 0.5$, and comparison data with Sousa et al. [12].

δ	u_{min}/U	Sousa et al.	v_{max}/U	Sousa et al.
0.1	−0.207607	−0.207663	0.182397	0.184589
0.5	−0.168859	−0.168899	0.145097	0.146735

on $x/L = 0.1$ respectively so as to progressively refine the mesh (h-refinement) between $0 \le x/L < 0.1$ and $0.9 < x/L \le 1$ for each increase in m. The polynomial order is varied between $N = 8$ and $N = 16$ (p-refinement) for the least resolved elemental mesh $m = 8$. Due to computational limitations only $N = 8$ and $N = 10$ are considered for $m = 16$, and $N = 8$ for $m = 20$. Fig. 2, demonstrates two representative simulation meshes with the same degrees of freedom but varied h- and p-refinement.

The fluid dynamic constants were set as Re $= 10^{-6}$ for the Newtonian study, Re $= 0$ and $\beta = 0.5$ for the viscoelastic studies and $\alpha = 0.001$ for the Giesekus model. The pressure integral coefficient is set to $\mu = 1$ across all simulations. The time step size was also varied to study the effect of temporal refinement, with the largest time step size at $\Delta t = 0.001$, which was sufficient for stability convergence to at least $S^n < \epsilon = 10^{-9}$ provided there was convergence in the constitutive system defined in Eq. (16). This is to be expected, since the CFL condition,

$$C = \Delta t \left(\sum_i \frac{|u_i|}{\Delta x_i} \right) \le C_{max}, \tag{35}$$

is satisfied for all meshes and lid velocity profiles considered with a time step of the order 10^{-3} or less, where C_{max} can be slightly higher than one for the semi-implicit method used in this study [22]. The maximum value of C in this study is approximately 0.5, which occurs in the mesh $m = 20$, $N = 8$ for time step $\Delta t = 0.001$ along the lid at $x/L = \delta$.

5.2. Newtonian

To ascertain the viscoelastic effects on the fluid flows by comparison with their Newtonian counterparts, a creeping Newtonian study was first performed in the limit Re $\to 0$ for $\delta = 0, 0.1$ and 0.5. Comparison of the data with the existing literature for finite volume studies, presented in Table 1, shows a majority agreement in the value of the minimum u velocity along x/L to within 0.06%, and between the value of the maximum v velocity along y/L to within 1.1%. The discrepancy between these results and those of Sahin and Owens [13] of approximately 2% for v/L may be due to their use of leaky boundary conditions at the corners to reduce the effect of the singularities.

Table 2 quantitatively shows how the strength of the primary vortex is reduced in the regularised regime, with the reduction in the magnitude of u_{min}/U being approximately 20% between $\delta = 0$, shown in Table 1, and $\delta = 0.5$. This quantity essentially shows the maximum speed of the lower edge of the vortex along the centre line, and thus the greater its magnitude, the stronger the vortex is. Regularisation $\delta = 0.1$ is thus shown to increase the vortex strength back towards the unregularised value, however from Fig. 3 one can see that the regularisations introduce an extensional flow along the lid which is not
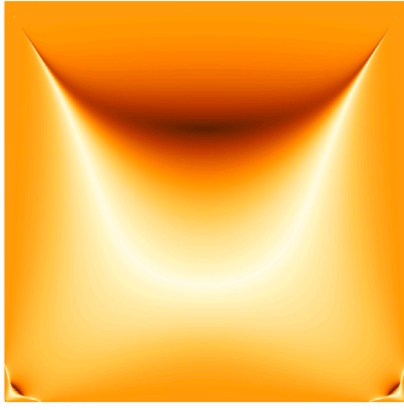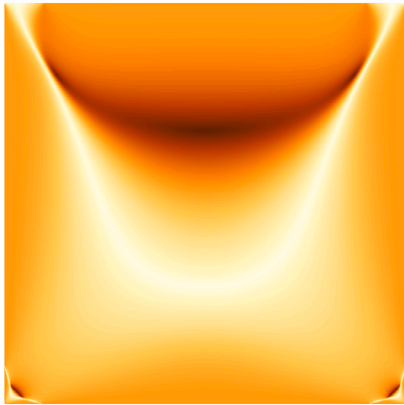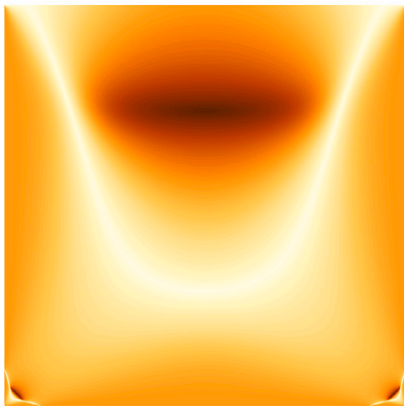
(a) $\delta = 0$

(b) $\delta = 0.1$

(c) $\delta = 0.5$

Fig. 3. Flow type parameter for creeping Newtonian flow. $\xi = 1$ (white) represents pure extensional flow, $\xi = 0$ (orange) represents pure shear flow and $\xi = -1$ (brown) represents solid-body rotation. $m = 20$, $N = 8$, $\Delta t = 0.001$.

present in the unregularised case, which is furthermore discontinuous along the lid in the $\delta = 0.1$ regularisation.
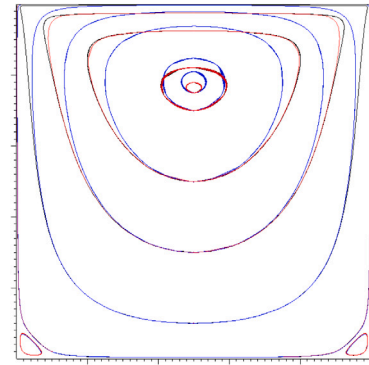

Fig. 4. Streamlines for the $\delta = 0, 0.1$ and 0.5 Newtonian flows. $\delta = 0$ is displayed in black, $\delta = 0.1$ in red and $\delta = 0.5$ in blue. $m = 20$, $N = 8$, $\Delta t = 0.001$.

By comparison of the streamlines presented in Fig. 4, one can see that qualitatively, the greater differences between each regularisation regime occur nearer the top two corners — as would be expected. In order to quantify these differences, one can introduce the local frame invariant flow type parameter ξ based on the criterion of Astarita [29] as $\xi = \frac{|\mathbf{d}| - |\mathbf{\Omega}|}{|\mathbf{d}| + |\mathbf{\Omega}|}$, where $|\mathbf{d}|$ and $|\mathbf{\Omega}|$ are the magnitudes of the rate of deformation tensor and the vorticity tensor respectively. Thus $\xi = 1$ represents pure extensional flow, $\xi = 0$ represents pure shear flow and $\xi = -1$ represents solid-body rotation. As shown in Fig. 3, the flow close to the walls is mainly shear-dominated, however in the regularised schemes the flow towards the top corners becomes more extensional due to the regions of local fluid acceleration. As this acceleration region becomes smaller ($\delta = 0.5 \rightarrow 0.1$), so does the region of extensional flow, approaching the unregularised flow field, whose extensional flow region is negligible at the wall-lid boundaries.

It is also worth noting the secondary Moffat vortices [5] visible in the lower two corners of Figs. 4 and 3(a)–3(c), inflated in Fig. 5, which do not depend on the regularisation scheme as their absolute size and distance from the corner are dependent only on the Reynolds number and the angle between the walls, which is identical in all cases. The relative sizes and centre distances from the corner of each subsequent vortex in the cascade are also dependent only on the angle between the walls. One can confirm that the distance of the centres of consecutive Moffat eddies from the corner drops off at a ratio of approximately $e^{2.8}$ between the secondary vortex and the tertiary vortex, as predicted for an internal angle of $\pi/2$ [5], however the mesh is not refined enough to resolve any vortices beyond this.

5.3. Oldroyd-B

The viscoelastic study of a broad range of regularisations δ, h-refinements, p-refinements, temporal refinements and Weissenberg numbers was performed by the running and analysis of over 400 simulations, and therefore it is sensible only to present some representative data resulting from the investigation which highlight the key features of interest in the most straightforward and concise way. To that effect, unless explicitly stated otherwise, the presented results utilise the mesh $m = 20$, $N = 8$ with time step $\Delta t = 0.001$.

Comparison of the data obtained in this study with the literature for an Oldroyd-B fluid is presented in Table 3 for the maximum value of the natural logarithm of the dimensionless quantity τ_{xx} on the centreline $x/L = 0.5$, with We $= 0.5$, and the positions of the centres of the primary vortices.

Elasticity serves to modify the velocity field, in particular by breaking the fore-aft symmetry about the centreline $x/L = 0.5$ as demonstrated by the shift in position of the primary vortex towards the upper-left corner with increasing We, as shown qualitatively by means of computed streamlines for $\delta = 0.5$ in Fig. 6 and quantified in
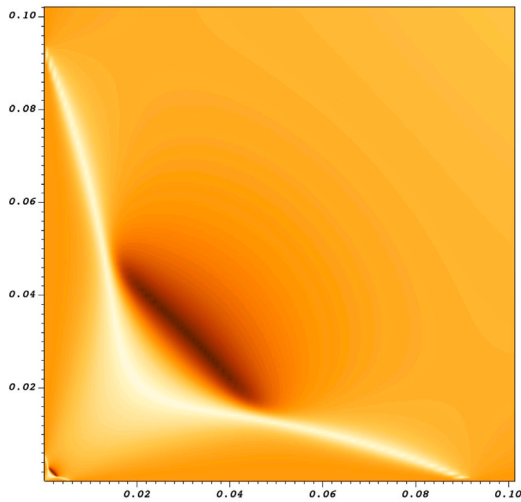
(a) First Moffat eddy (secondary vortex), a close-up of the bottom left corner of figure 3a.
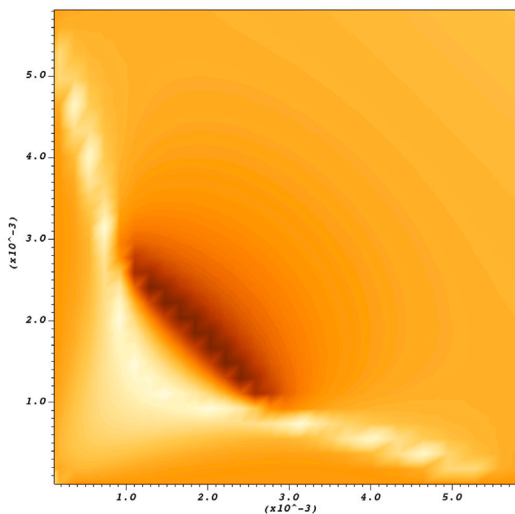
(b) Second Moffat eddy (tirtiary vortex), a close-up of the bottom left corner of figure 5a.

Fig. 5. First two Moffat eddies for the unregularised Newtonian fluid, visualised using the flow type parameter ξ.

Fig. 6. Streamlines for $\delta = 0.5$: black for Newtonian, yellow for We = 0.2, red for We = 0.4 and blue for We = 0.6.

Table 3
Comparison of representative results with literature for Oldroyd-B model with $\delta = 0.5$, $\beta = 0.5$, Re $= 0$ and We $= 0.5$.

Reference	We	MAX$(\ln \tau_{xx}(x=0.5))$	x_c/L	y_c/L
Pan et al. [10]	0.5	≈ 5.5	0.469	0.798
Sousa et al. [12]	0.5	5.57	0.467	0.801
Present study	0.5	5.55	0.468	0.799

Table 4
Centre of the primary vortex for a representative range of We and δ.

δ	We	x_c/L	y_c/L
0.1	0.05	0.500	0.765
0.1	0.1	0.498	0.767
0.1	0.15	0.495	0.770
0.5	0.2	0.494	0.786
0.5	0.4	0.474	0.794
0.5	0.6	0.461	0.803

Table 5
Velocity profile data for a range of hp-refinements with $\delta = 0.1$ and We $= 0.15$.

m	N	u_{min}/U	$y_{min/L}$	v_{max}/U	x_{max}/L
8	8	−0.199988	0.53675	0.174255	0.20850
8	10	−0.199876	0.53675	0.174117	0.20850
8	12	−0.199901	0.53675	0.174147	0.20850
8	14	−0.199909	0.53675	0.174156	0.20850
8	16	−0.199902	0.53675	0.174146	0.20850
16	8	−0.199935	0.53909	0.175953	0.20539
16	10	−0.199933	0.53909	0.175950	0.20539
10	8	−0.199934	0.53858	0.175970	0.20540

Table 6
Maximum attainable Weissenberg number for varying number of elements and polynomial order for regularisation $\delta = 0.1$. The distance between the wall and the first GLL point is $\Delta x_{0,GLL}$, while the average resolution in the first element is $\Delta x_{0,avg}$; these give an indication of the spatial resolution in the region of rapid stress growth.

m	N	$\Delta(x/L)_{0,GLL}$	$\Delta(x/L)_{0,avg}$	We$_{max}$
8	8	0.00142	0.00354	0.16
8	10	0.00093	0.00283	0.18
8	12	0.00066	0.00235	0.20
8	14	0.00049	0.00202	0.21
8	16	0.00038	0.00177	0.22
16	8	0.00054	0.00135	0.21
16	10	0.00036	0.00108	0.21
20	8	0.00016	0.00040	0.19

Table 4. This is in agreement with the experimental work of Pakdel et al. [7,30,31], who performed studies on the creeping flow of two Boger fluids [32]. The flow type parameter for the Oldroyd-B fluid with $\delta = 0.5$ is shown in Fig. 7, further demonstrating the greater breaking of fore-aft symmetry with increasing We. It can also be seen that the flow is significantly affected by the increase in We close to the lid by comparison with each regularisation's Newtonian counterpart, shifting the region of pure extension on the lid away from the top-left (upstream) corner.

A study into the effects of elemental and spectral refinement was performed for the Oldroyd-B fluid with the regularisation $\delta = 0.1$ and time step size $\Delta t = 0.001$. Table 5 shows that the We $= 0.15$ velocity fields for each of the GLL meshes are virtually identical. Table 6 shows the maximum attainable Weissenberg numbers alongside quantities representative of the level of elemental and spectral refinement (known as hp-refinement) at the walls, with $\Delta(x/L)_{0,GLL}$ being the distance
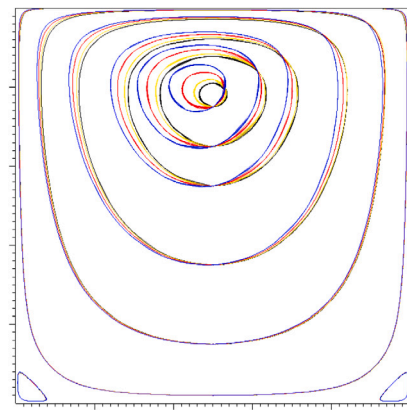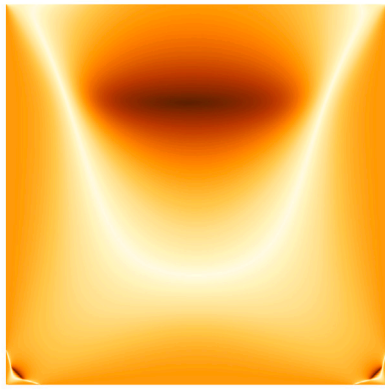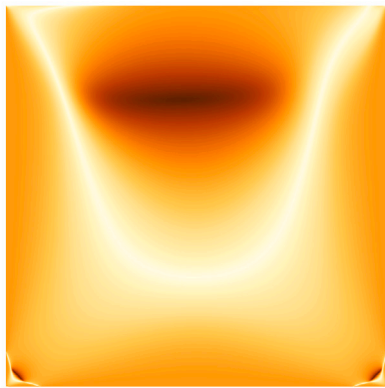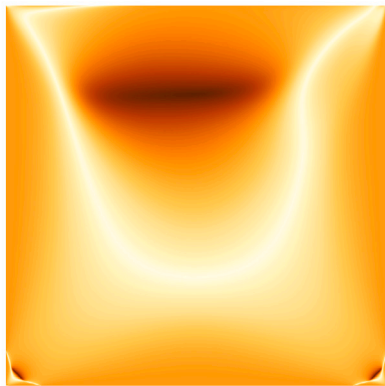
(a) We=0.2

(b) We=0.4

(c) We=0.6

Fig. 7. Flow type parameter for an Oldroyd-B fluid, with $\delta = 0.5$ and We from 0.2 to 0.6.

between the wall and the first GLL point and $\Delta(x/L)_{0,avg}$ being the average resolution within the first element. One can see that for meshes with an identical number of degrees of freedom ($m = 8, N = 16$ and

$m = 16, N = 8$; $m = 16, N = 10$ and $m = 20, N = 8$), those with the higher polynomial order are better resolved near the elemental boundaries, where the features of interest reside at the wall and $C1$ discontinuity, due to the non-uniformity of the GLL points. It is clear from these data that higher spatial resolution through a combination of elemental and spectral refinement plays a role in increasing the maximum attainable Weissenberg number, implying that this quantity is one of numerical origin, rather than a representation of the physical onset of elastic instability.

The breakdown of the flow in the present study occurs prior to the absence of a steady state solution due to divergence in the BDF/FPI constitutive system above a maximum Weissenberg number We_{max} which is dependent on the level of hp-refinement. This implies the compounding of errors in the iterative scheme, which are seen to be reduced by means of refinement allowing higher Weissenberg numbers to be reached; Mendelson et al. [33] indeed ruled out the loss of steady, two-dimensional flow fields by the existence and uniqueness of the solution to a second-order fluid in a driven cavity, attributing the numerical breakdown of a finite element method to the error in stress gradient approximation. While the addition of the p-refinement that separates the spectral element method from the finite element method does enable a more accurate method of capturing the stress gradient, it is logical to conclude that it fails for the same reason. The implication therefore is that in order to continue raising the Weissenberg number, one must perform ever increasing hp-refinement, which in turn will demand ever increasing computational resources; however, the methodology is still shown to be very successful for sub-maximal Weissenberg numbers even at low resolutions. The maximum attainable Weissenberg numbers of the present study for the two regularisations $\delta = 0.5$ and $\delta = 0.1$ with $m = 20$, $N = 8$ and $\Delta t = 0.001$ are, respectively, 0.81 and 0.19; for a similar level of spatial and temporal refinement, Sousa at al reported maximum Weissenberg numbers of 0.63 and 0.18 under the same regularisation schemes [12].

While the $\delta = 0.1$ regularisation drives the bulk flow closer to the unregularised case than $\delta = 0.5$, the choice of regularisation scheme leaves a discontinuity in the velocity gradients, which in the non-Newtonian instance leads to discontinuities in the stress gradients. While the present methodology succeeds in recreating the results of Sousa et al. [12] and even achieving higher Weissenberg numbers, these discontinuities are naturally unphysical, and for this reason in the analysis of the elastic stresses the $\delta = 0.1$ regularisation is omitted. Fig. 8 shows the effect of increasing Weissenberg number on the elastic stress tensor components for regularisation $\delta = 0.5$, for the mesh $m = 20$, $N = 8$. A full assessment of the stress tensor component profiles was performed for all mesh refinements used in this study in this regularisation, and it was found that for refinements beyond $m = 8$, $N = 14$, with We = 0.5, their profiles overlap exactly. Therefore, in continuing the analysis with the $m = 20$, $N = 8$ mesh, there is confidence that this is well enough refined. However, it is noted in Fig. 8 that the downstream peaks become much steeper with increasing We, such that in the limiting case approaching the maximum attainable Weissenberg number the specific levels of hp-refinement will play a significant role, as previously observed for $\delta = 0.1$ in Table 6.

The presence of the regularisation alters dramatically the structure of the flow type parameter, in particular as without regularisation the flow experienced by the polymers along the lid would be of pure shear (see Fig. 3 for the changes at various regularisations for a Newtonian flow). Namely, the introduction of the variation of the horizontal velocity along the lid introduces a strong elongational flow in the two top corners of the cavity, which changes the structure of the flow type parameter. For these reasons the primary peak in the τ_{xx} component appears in the position where the extensional flow caused by the boundary conditions ceases - this can be inferred to occur in any regularisation considered in this study, as all possess regions of positive and negative acceleration. It is worth mentioning that the peak is not exactly central because the extensional flow is modulated
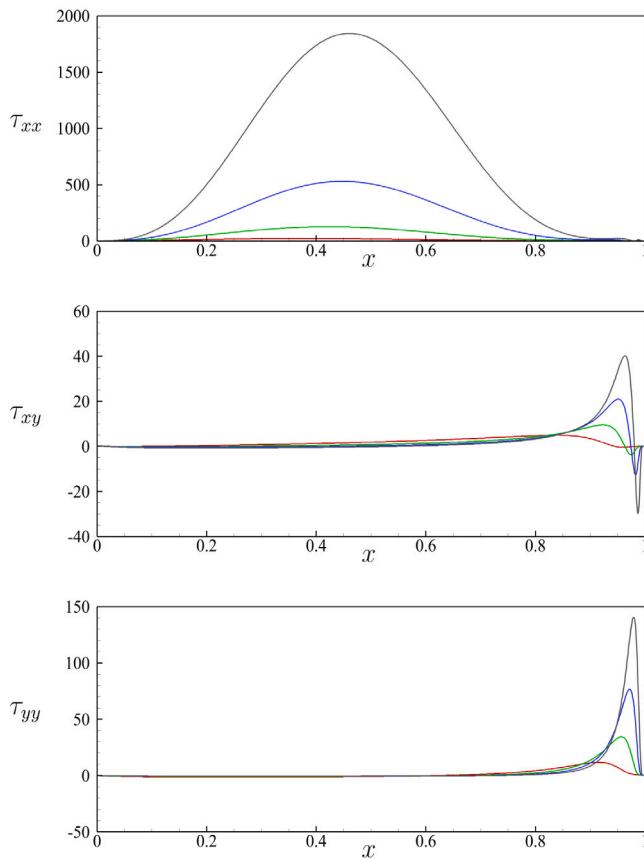
Fig. 8. Components of the elastic stress tensor $\boldsymbol{\tau}$ along the lid $y = 1$ with $\delta = 0.5$ for $We = 0.2$ (red), $We = 0.4$ (green), $We = 0.6$ (blue) and $We = 0.8$ (black).

Fig. 9. Components of the x-derivatives of the elastic stress tensor $\boldsymbol{\tau}$ contributing to $\boldsymbol{\nabla} \cdot \boldsymbol{\tau}$ along the lid $y = 1$ with $\delta = 0.5$ for $We = 0.2$ (red), $We = 0.4$ (green), $We = 0.6$ (blue) and $We = 0.8$ (black).

Table 7
Maximum attainable Weissenberg number for varying time step size and regularisation, mesh $m = 20$, $N = 8$.

δ	Δt	We_{max}
0.1000	0.001	0.19
0.1000	0.0001	0.26
0.0811	0.001	0.14
0.0811	0.0001	0.24
0.0592	0.001	0.09
0.0592	0.0001	0.16
0.0336	0.001	0.04
0.0336	0.0001	0.07

Table 8
Velocity profile data for the Oldroyd-B and Giesekus fluids for a range of mobility parameters α at We = 0.81.

Model	u_{min}/U	v_{max}/U	x_c	y_c
Oldroyd-B	−0.116970	0.112206	0.44683	0.81087
$\alpha = 0.0001$	−0.117124	0.112289	0.44684	0.81087
$\alpha = 0.001$	−0.118321	0.112959	0.44684	0.81087
$\alpha = 0.01$	−0.124435	0.116391	0.46013	0.86415

by the shear that is also experienced on the lid. The values of τ_{xx} increase sharply with increasing Weissenberg number. The presence of the shear at the lid is also responsible for the large values of the shear stress τ_{xy} that are observed near the top right corner of the domain, see the middle panel of Fig. 8, where it is shown to have a single sharp peak-trough feature in this region. It is worth mentioning that the observed values increase in magnitude with Weissenberg number for both regularisations. One can argue that these behaviours are all related to the large extensions achieved in the first part of the lid during the stretching. Furthermore, the sharply increasing oscillations and peaks in the τ_{xy} and τ_{yy} components respectively will inevitably lead to greater difficulty in accurately determining the stress gradients, which may contribute to the breakdown of the BDF/FPI scheme at higher Weissenberg numbers.

Further insight is gained by the direct assessment of the stress gradients, which are coupled with the momentum equation via the term $\boldsymbol{\nabla} \cdot \boldsymbol{\tau}$. It is evident from Fig. 9 that the magnitude of the oscillations in all elastic stress component derivatives increase sharply with increasing Weissenberg number, while the distance over which these oscillations occur decreases. It is therefore clear that beyond a certain Weissenberg number dependent on the resolution in this region, the spectral decomposition will indeed be unable to accurately capture these stress gradients.

Temporal refinement was also shown to increase the maximum attainable Weissenberg number across a range of regularisations, as displayed in Table 7. The elastic stresses for flows of the same Weissenberg number were identical for the two temporal refinements reported, suggesting that the increase in maximum attainable Weissenberg number is due to a reduction in the compounding of errors in the BDF/FPI system, preventing divergence at the higher Weissenberg numbers.
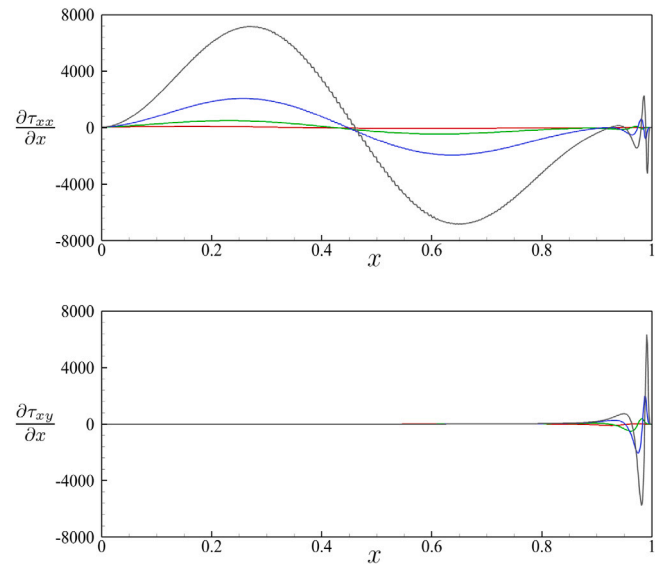
Further temporal refinement was performed, but this only marginally increased the maximum attainable Weissenberg number at the cost of substantially greater computation time.

The sole contribution of the stress gradients to the breakdown of the BDF/FPI scheme can be confirmed by returning to Eq. (16). In the Oldroyd-B scheme $\alpha = 0$, the only iterative contribution to $\tilde{\tau}^{i+1}$ is the term $-We(\mathbf{u}^{n+1} \cdot \boldsymbol{\nabla}\tilde{\tau}^i)$, for which in turn only the stress gradient is iterated. Therefore any compounding of errors that lead to the divergence of the scheme must come from the gradients of the stress tensor.

5.4. Giesekus

Since the Giesekus model rheologically reduces the extensional viscosity, it was worth investigating the Giesekus fluid with $\alpha = 0.01$, 0.001 and 0.0001 and comparing the results with those of the Oldroyd-B fluid. Fig. 10 demonstrates that the flow types between the Oldroyd-B and $\alpha = 0.001$ rheologies are close to identical, barring a minor difference in the extensional flow near the top-right corner. The velocity
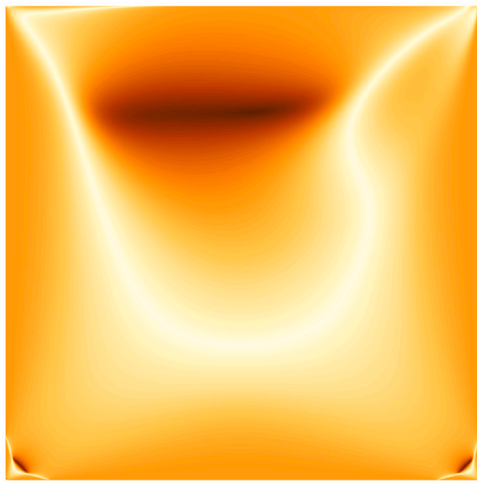
(a) Oldroyd-B
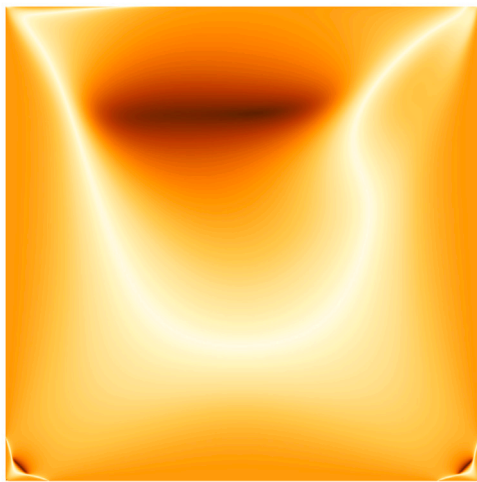
(b) Giesekus

Fig. 10. Flow type parameter for an Oldroyd-B fluid and a Giesekus fluid with $\alpha = 0.001$ for regularisation $\delta = 0.5$ at the maximum attainable Weissenberg number for the Oldroyd-B fluid in this regularisation, We $= 0.81$.

Fig. 11. Stress tensor components along the lid for the Oldroyd-B and Giesekus fluids with $\alpha = 0.01$, 0.001 and 0.00010 for regularisation $\delta = 0.5$ at the maximum attainable Weissenberg number for the Oldroyd-B fluid in this regularisation, We $= 0.81$.

Fig. 12. Elastic stress x-derivatives along the lid $y/L = 1$ near the downstream wall $x/L = 1$ for the Oldroyd-B (red) and Giesekus fluid $\alpha = 0.001$ (green) with $\delta = 0.5$ at their respective maximum Weissenberg numbers, We$_{max,Old} = 0.81$ and We$_{max,Gie} = 1.33$.

fields are also shown in Table 8 to be virtually identical between the two rheological models up to $\alpha = 0.01$, whereupon the primary vortex becomes marginally stronger and its centre shifts moderately towards the $x = 0.5$ centreline and towards the lid.

Across a range of mobility parameters, the elastic stress components, shown in Fig. 11, are reduced by comparison with their Oldroyd-B counterpart with increasing α. It can be seen that the effect of this is incredibly slight for $\alpha = 0.0001$, and drastically more pronounced for each tenfold increase. There is also a greater breaking of the fore-aft symmetry along the velocity-regularised lid, skewing all peaks slightly towards the upstream corner $x = 0$. This behaviour is also displayed in the gradients of the elastic stress components, here not shown, reducing the peaks in the downstream corner oscillations and also stretching them slightly in the upstream direction, making them easier to resolve at this Weissenberg number. This leads to a higher
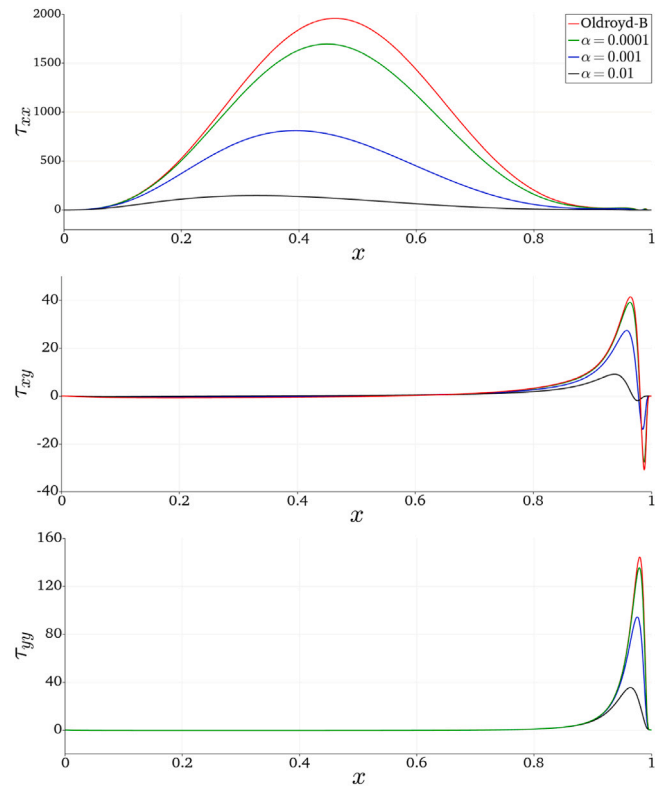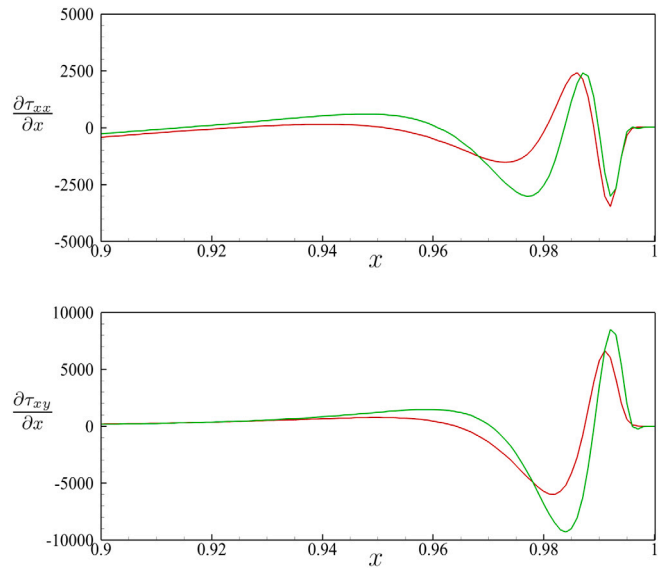
maximum attainable Weissenberg number for the Giesekus fluid than the Oldroyd-B fluid, for example in the $\alpha = 0.001$ case, We$_{max,Gie} = 0.33$ for $\delta = 0.1$ and We$_{max,Gie} = 1.33$ for $\delta = 0.5$. Components of the stress gradient for the Oldroyd-B and Giesekus fluid with $\alpha = 0.001$ at their respective maximum Weissenberg numbers are plotted in Fig. 12 for the $\delta = 0.5$ regularisation to demonstrate that the stress gradients are similar for both rheologies at their maximum attainable Weissenberg

numbers, suggesting that the same breakdown mechanism occurs for both rheologies.

6. Conclusions

A systematic analysis of the performance of a DEVSS-G spectral element method for simulating a non-Newtonian flow was performed by means of the study of a square lid-driven cavity. The method was first validated by assessing the creeping Newtonian flow of the idealised lid-driven cavity, showing excellent agreement with the literature. In the non-Newtonian regime, the singularity due to the discontinuous velocity boundary conditions on the lid-wall interfaces meant that the idealised cavity could not be assessed. The existing literature utilised a quartic regularisation scheme to navigate this, guaranteeing zero velocity and velocity gradient on the lid-wall interfaces, and the present study again showed excellent quantitative agreement with existing numerical studies, and qualitatively behaved as per the experimental studies of Boger fluids. The methodology of the present study was able to obtain higher Weissenberg numbers than the existing literature; Sousa et al. [12] obtained maximum Weissenberg numbers of 0.63 and 0.18 for the $\delta = 0.5$ and 0.1 quartic regularisations respectively, while the present study was able to achieve Weissenberg numbers of 0.81 and 0.19 at similar levels of temporal and spatial refinement for the Oldroyd-B fluid. The effects of changing the Weissenberg number, the regularisation parameter δ, the level of hp-refinement and temporal refinement were all studied over a large number of simulations. The breakdown of the numerical system was shown to occur in all cases before the breakdown of a steady-state solution, owing to the inability to accurately resolve the high stress gradients. This led to a compounding of errors in the BDF/FPI time advancement scheme, ultimately causing the methodology to become unstable. This was further shown by briefly considering the Giesekus extension to the Oldroyd-B model; for a range of mobility parameters α, the resulting progressively shallower stress gradients predicted with increasing α enabled the Weissenberg numbers to be increased across all regularisations, before the same breakdown eventually occurred. This difficulty in accurately resolving the steep stress gradients implies that the methodology would not be effective in the study of, for example, purely elastic turbulence in the 2D lid driven cavity, without significantly greater hp-refinement in order to fully and accurately resolve these gradients.

CRediT authorship contribution statement

D. Fenton: Writing – review & editing, Writing – original draft, Visualization, Methodology, Investigation, Formal analysis, Data curation, Conceptualization. **P.J. Bowen:** Writing – review & editing, Validation, Supervision, Resources, Conceptualization. **E. De Angelis:** Writing – review & editing, Visualization, Validation, Supervision, Resources, Methodology, Conceptualization.

Declaration of competing interest

The authors declare that they have no known competing financial interests or personal relationships that could have appeared to influence the work reported in this paper.

Data availability

Data will be made available on request.

Acknowledgments

References

[1] M. Kawaguti, Numerical solution of the navier-stokes equations for the flow in a two-dimensional cavity, J. Phys. Soc. Jpn. 16 (1961).

[2] O. Botella, R. Peyret, Benchmark spectral results on the lid-driven cavity flow, Comput. & Fluids 27 (1998).

[3] U. Ghia, K.N. Ghia, C.T. Shin, High-re solutions for incompressible flow using the navier-stokes equations and a multigrid method, J. Comput. Phys. 48 (1982).

[4] J.R. Koseff, R.L. Street, The lid-driven cavity flow: A synthesis of qualitative and quantitative observations, J. Fluids. Eng. 106 (1984).

[5] H.K. Moffat, Viscous and resistive eddies near a sharp corner, J. Fluid Mech. 18 (1964).

[6] C.K. Audun, A. Triantafillopoulos, J.D. Benson, Global stability of lid-driven cavity with throughflow: flow visualisation studies, Phys. Fluids A 3 (1996).

[7] P. Pakdel, G.H. McKinley, Elastic instability and curved streamlines, Phys. Rev. Lett. 77 (1996).

[8] K. Yapci, B. Karasozen, Y. Uludag, Finite volume simulation of viscoelastic laminar flow in a lid-driven cavity, J. Non-Newton. Fluid Mech. 164 (2009).

[9] F.P. Martins, C.M. Oishi, A.M. Afonso, M.A. Alves, A numerical study of the kernel-conformation transformation for transient viscoelastic fluid flows, J. Comput. Phys. 302 (2015).

[10] T.W. Pan, J. Hao, R. Glowinski, On the simulation of a time-dependent cavity flow of an oldroyd-b fluid, Internat. J. Numer. Methods Fluids 60 (2009).

[11] A.M. Grillet, B. Yang, B. Khomami, E.S.G. Shaqfeh, Modelling of viscoelastic lid-driven cavity flows using finite element simulations, J. Non-Newton. Fluid Mech. 88 (1999).

[12] R.G. Sousa, R.J. Poole, A.M. Afonso, F.T. Pingo, P.J. Oliveira, A. Morozov, M.A. Alves, Lid-driven cavity flow of viscoelastic liquids, J. Non-Newton. Fluid Mech. 234 (2016).

[13] R.G. Sahin, M, Owens, A novel fully implicit finite volume method applied to the lid-driven cavity problem, part i: high reynolds number flow calculations, Internat. J. Numer. Methods Fluids 42 (2003).

[14] R.D. Henderson, Dynamic refinement algorithms for spectral element methods, Comput. Methods Appl. Mech. Eng. 175 (1999).

[15] R.M. Kynch, T.N. Phillips, A high resolution spectral element approximation of viscoelastic flows in axisymmetric geometries using a DEVSS-G/DG formulation, J. Non-Newton. Fluid Mech. 240 (2017).

[16] D. Rh. Gwynllyw, T.N. Phillips, On the enforcement of the zero mean pressure condition in the spectral element approximation of the stokes problem, Comp. Methods Appl. Mech. Eng. 195 (2006).

[17] J.G. Oldroyd, On the formulation of rheological equations of state, Proc. R. Soc. Lond. Ser. A Math. Phys. Eng. Sci. 200 (1950).

[18] H. Giesekus, A simple constitutive equation for polymer fluids based on the concept of deformation-dependent tensorial mobility, J. Non-Newton. Fluid Mech. 11 (1982).

[19] A.W. Liu, D.E. Bornside, R.C. Armstrong, R.A. Brown, Viscoelastic flow of polymer solutions around a periodic, linear array of cylinders: comparisons of predictions for microstructure and flow fields, J. Non-Newton. Fluid Mech. 77 (1998).

[20] A.C.B. Bogaerds, A.M. Grillet, G.W.M. Peters, F. Baaijens, Stability analysis of polymer shear flows using the extended pom-pom constitutive equations, J. Non-Newton. Fluid Mech. 108 (2002).

[21] Y. Maday, A.T. Patera, M. Ronquist, An operator-integration-factor splitting method for time-dependent problems: application to incompressible fluid flow, J. Sci. Comput. 5 (1990).

[22] R. Courant, K. Friedrichs, H. Lewy, Über die partiellen differenzengleichungen den mathematischen physik, Math. Ann. 100 (1928).

[23] W.J. Gordon, C.A. Hall, Transfinite element methods: blending function interpolation over arbitrary curved element domains, Numer. Math. 21 (1973).

[24] C. Schneidesch, M.O. Deville, Chebyshev collocation method and mulit-domain decomposition for navier-stokes equations in complex curved geometries, J. Comput. Phys. 105 (1993).

[25] F. Belblidia, H. Matallah, M. Webster, Alternative subcell discretisations for viscoelastic flow: velocity-gradient approximation, J. Non-Newton. Fluid Mech. 151 (2008).

[26] P. Lesaint, P.A. Raviart, On a Finite Element Method for Solving the Neutron Transport Equation, Univ. Paris VI, Labo. Analyse Numerique, 1974.

[27] M. Fortin, A. Fortin, A new approach for the fem simulation of viscoelastic flows, J. Non-Newton. Fluid Mech. 32 (1989).

[28] R.G. Owens, T.N. Phillips, Computational Rheology, Imperial College Press, 2002.

[29] G. Astarita, Objective and generally applicable criteria for flow classification, J. Non-Newton. Fluid Mech. 6 (1979).

[30] P. Pakdel, S.H. Spiegelberg, G.H. McKinley, Cavity flow of viscoelastic fluids: two dimensional flows, Phys. Fluids 9 (1997).

[31] P. Pakdel, G.H. McKinley, Cavity flows of elastic liquids: purely elastic instabilities, Phys. Fluids 10 (1998).

[32] D.V. Boger, A highly elastic constant-viscosity fluid, J. Non-Newton. Fluid Mech. 3 (1977).

[33] M.A. Mendelson, P.W. Yeh, R.A. Brown, R.C. Armstrong, Approximation error in finite element calculation of viscoelastic fluid flows, J. Non-Newton. Fluid Mech. 10 (1982).